Research Square

Preprints are preliminary reports that have not undergone peer review.
They should not be considered conclusive, used to inform clinical practice,
or referenced by the media as validated information.

XPR1 prevents T-cell hyperactivation through interaction with KIDINS220 for endocytic regulation of CD28 costimulation

Reiner Mailer

r.mailer@uke.de

University Medical Center Hamburg-Eppendorf https://orcid.org/0000-0001-8279-3355

Marion Mengel

University Medical Center Hamburg-Eppendorf

Benita Kröger

University Medical Center Hamburg-Eppendorf

Mandy Malle

University Medical Center Hamburg-Eppendorf

Maike Frye

University Medical Center Hamburg-Eppendorf

Thomas Renne

University Medical Center Hamburg-Eppendorf

Timur Yorgan

University Medical Center Hamburg-Eppendorf

Björn-Philipp Diercks

University Medical Centre Hamburg-Eppendorf

Article

Keywords: XPR1, CD28 costimulation, KIDINS220, CD4+ T cells, cytokines, activation pathways

Posted Date: September 26th, 2026

DOI: https://doi.org/10.21203/rs.3.rs-11036225/v1

License: This work is licensed under a Creative Commons Attribution 4.0 International License.
Read Full License

Additional Declarations: (Not answered)

Abstract

Together with T-cell antigen receptor (TCR) engagement, CD28 costimulation is a central process that defines T-cell proliferation and differentiation relevant for immunotherapy. Here, we show that xenotropic and polytropic retrovirus receptor 1 (XPR1) regulates activation pathways and cytokine expression in CD4+ T cells by restricting CD28 costimulation. T cell-specific *Xpr1* gene deletion, abrogated TCR-mediated Ca^{2+}/NFAT signaling but enhanced AKT/mTOR pathway activation, resulting in impaired thymocyte development and hyperactivated CD4+ T cells in the periphery. Consistently, XPR1 deficiency led to increased cytokine expression in CD4+ T cells from TCR-transgenic mice and Jurkat cells. Mechanistically, XPR1 associates with kinase D-interacting substrate of 220 kDa (KIDINS220) in CD4+ T cells and regulates membrane rearrangement, CD28 surface clustering and CD28 costimulation-dependent proliferation. Utilizing membrane-permeable peptides to interfere with XPR1-KIDINS220 interactions, transcriptome analysis identified XPR1 as regulator for endocytosis and corroborated that XPR1 targeting has immunomodulatory functions for CD28 costimulation in human CD4+ T cells.

INTRODUCTION

Xenotropic and polytropic retrovirus receptor 1 (XPR1) is a 10-pass transmembrane protein that is implicated in cellular phosphate and Ca^{2+} homeostasis. Mutations of human XPR1 are associated with primary familiar brain calcification (PFBC), a neurodegenerative disease characterized by abnormal calcium deposits in the basal ganglia region [1]. While global *Xpr1* deletion causes embryonic and perinatal lethality in mice [2], monoallelic *Xpr1* deletion leads to vascular calcification in combination with microgliosis and immune pathway activation [3, 4]. Corroborating a role in cytokine signaling, the lack of XPR1 in hematopoietic progenitors promotes interferon-activated monocyte/macrophage differentiation but fails to sustain macrophage development in fetal liver [5].

Central for cytokine expression in T-cell antigen receptor (TCR)-stimulated T cells is the strength of costimulation [6]. Facilitated by CD28 ligation on the plasma membrane of T cells with CD80 and CD86 on the surface of activated APCs, costimulation signaling elicits proliferation, interleukin (IL)-2 production and promotes pro-inflammatory cytokine expression via AKT/mTOR pathway activation [7–9]. Under septic conditions, excessive costimulation can initiate cytokine release syndrome that culminates in life-threatening organ failure [10], whereas unimpeded CD28 signaling has emerged as important molecular mechanism for immune checkpoint inhibitor treatment in cancer immunotherapy [11, 12]. Thus, mechanistic regulators of CD28 costimulation are potential targets for clinical immunomodulation.

Here, we identified XPR1 as adapter protein that restricts CD28-dependent proliferation, cytokine expression and AKT/mTOR activation in CD4 + T cells. Costimulation of XPR1-deficient CD4 + T cells resulted in hyperproliferation, aberrant membrane rearrangement and elevated antigen-specific Th17 differentiation *in vivo*. *Vice versa*, XPR1-deficient CD4 + T cells showed reduced homeostatic expansion under CD28-independent conditions with decreased TCR-mediated Ca^{2+} mobilization and impaired

thymic development. Utilizing membrane-permeable peptides, we revealed that competitive inhibition of the association with Kinase D-interacting substrate of 220 kDa (KIDINS220) intensifies CD28 surface staining and enhances proliferation. Together, we found that XPR1 regulates CD28 costimulation in CD4 + T cells via KIDINS220-mediated endocytosis pathways.

RESULTS

XPR1-deficient CD4+ T cells are hyperactivated

XPR1 contributes to the formation of supramolecular complexes and potentially regulates secondary messenger during signaling processes [13-16]. To investigate XPR1-dependent immune cell signaling, we analyzed conditional *Xpr1* knockout mice with T cell-specific deletion using CD4-Cre transgenic mice (Fig. 1A, Fig. S1). In comparison to control (CTL, $Xpr1^{fl/fl}$) and conditional heterozygous (cHET, $Cd4\text{-}Cre^{+}$ $Xpr1^{wt/fl}$) littermates, conditional XPR1 knockout mice (cKO, $Cd4\text{-}Cre^{+}$ $Xpr1^{fl/fl}$) showed an impaired maturation of thymocytes, marked by decreased single positive populations (Fig. 1B). We found that XPR1 deficiency leads to a developmental blockade of CD44-CD25+ thymocytes at the DN3 stage (Fig. 1C) with fewer recently selected CD69+TCRb+ and CD5+ DP thymocytes (Fig. 1, D and E), suggesting an insufficient thymic selection of thymocytes lacking XPR1 [17,18].

Consequently, peripheral T-cell populations were reduced in size and absolute T-cell numbers decreased in XPR1 cKO mice compared to cHET and CTL mice (Fig. 1F and Fig. S2). However, CD4+ T cells lacking XPR1 displayed increased populations of CD44+CD62L- effector memory T cells (Fig. 1G) and expressed higher levels of CD71, CTLA-4 and Ki-67 *ex vivo* (Fig. 1, H and I, Fig. S3), indicating recent T-cell activation, exhaustion and proliferation, respectively. To assess XPR1-dependent hyperstimulation, we isolated naïve CD4+ T cells from XPR1 cKO and CTL mice and analyzed their proliferation following anti-CD3/anti-CD28 stimulation *in vitro*. XPR1 deficiency enhanced T-cell proliferation (Fig. 1J), suggesting that XPR1 regulates signaling pathways in CD4+ T cells.

Genetic deletion of *Xpr1* in tubular epithelial cells leads to phosphaturia and renal dysfunction [2], while abrogation of XPR1-mediated phosphate export in platelets has been shown to accumulate inorganic polyphosphate [19]. Recently, we found that polyphosphate degradation in CD4+ T cells via exogenous enzyme transfer triggers T-cell hyperactivation (Kröger B, 2025, unpubl. data). To test whether altered polyphosphate levels play a role in hyperproliferation of T cells without XPR1 expression, we analyzed purified polyphosphate isolated from CD4+ T cells with *Xpr1* gene deletion. In comparison, size distribution and amount of polyphosphate were similar between groups (Fig. S4), suggesting enhanced proliferation of XPR1-deficient CD4+ T cells depends on other protein functions than phosphate channeling.

Xpr1 deletion increases IL-2 independently of Ca^{2+}/ERK signaling in CD4+ T cells

To gain insight into differential pathway activation mediated by XPR1 deficiency, we analyzed expression profiles of naïve CD4+ T cells from XPR1 cKO and CTL mice after 6 h anti-CD3/anti-CD28 stimulation (Fig. 2A). Among early transcriptional changes that differed significantly in response to XPR1 deficiency were 60 up- and downregulated genes encompassing TCR-related genes (Fig. S5A), which confirms the aforementioned impaired thymic development (Fig. 1, B-D), and genes associated with pathways for interleukin signaling and inflammation mediated by chemokine and cytokine signaling (Fig. 2A and Fig. S5B). RNA microarrays revealed a 23.2-fold increase for *Il2* transcripts in stimulated CD4+ T cells from XPR1 cKO compared to CTL mice, implying XPR1 impacts on T-cell stimulation responsiveness. Measuring intracellular Ca^{2+} concentrations by time-lapse microscopy, we found that XPR1 deficiency reduced Ca^{2+} fluxes in naïve CD4+ T cells stimulated with anti-CD3 and thapsigargin treatment (Fig. 2B and Fig. S6). Consistently, ERK-mediated signaling was decreased in naïve CD4+ T cells lacking XPR1 in response to TCR stimulation (Fig. 2C). Notably, both ERK isoforms displayed reduced phosphorylation in XPR1-deficient CD4+ T cells and could not be compensated by heterozygous XPR1 expression (Fig. S7). In addition, nuclear translocation of NFAT was impaired in XPR1-deficient CD4+ T cells treated with anti-CD3 or ionomycin, further demonstrating defective Ca^{2+}/ERK/NFAT signaling in the absence of XPR1 (Fig. 2D, Fig. S8). Nevertheless, long-term stimulation elicited hyperstimulation in naïve CD4+ T cells from XPR1 cKO mice in comparison to CTL mice, indicated by higher CD44 and CD25 expression levels and increased IL-2 secretion (Fig. 2, E and F).

XPR1 deficiency promotes AKT/mTOR signaling and cytokine production

Next, we investigated AKT/mTOR pathway activation to clarify how XPR1 deficiency promotes IL-2 expression at the transcriptional and protein level. Naive CD4+ T cells from XPR1 cKO mice increased AKT and S6 phosphorylation in response to TCR stimulation compared to those from cHET and CTL mice (Fig. 3, A and B, Fig. S9). In line with the notion that AKT/mTOR signaling drives pro-inflammatory cytokine production in CD4+ T cells [20,21], XPR1-deficient T cells increased TNF-a and IFN-g expression and IL-17a and IL-22 expression under Th1- and Th17-skewing conditions, respectively (Fig. 3, C and D). Accompanied by elevated IL-2 production in both differentiation settings, however, lineage-specific transcription factors T-bet and RORgt were not induced in CD4+ T cells from XPR1 cKO mice compared to CTL mice (Fig. 3, C and D and Fig. S10A). Likewise, XPR1-deficient CD4+ T cells showed reduced expression of FOXP3 *in vitro* and GATA3 *ex vivo* (Fig. S10, A and B). To compare antigen-specific responses in naïve CD4+ T cells with or without XPR1 expression *in vivo*, we crossed *Cd4-Cre*$^{+}$ *Xpr1*$^{fl/fl}$ and *Cd4-Cre*$^{-}$ *Xpr1*$^{fl/fl}$ with TCR-transgenic *Marilyn* mice [22] to generate a line with conditional *Xpr1* gene deletion in TRBV6+ T cells that recognize male H-Y antigen on a *Rag2*$^{-/-}$ background (XPR1 cKO *Marilyn* and CTL *Marilyn*, respectively). Following intravenous injection of the cognate male H-Y antigen epitope into female recipients, we analyzed expression profiles of TCR-transgenic CD4+ T cells from XPR1 cKO *Marilyn* and CTL *Marilyn* mice by flow cytometry (Fig. 3E). Proliferation marker Ki-67, exhaustion marker PD-1 and CTLA-4 as well as IL-17a and IL-22 cytokine expression increased in CD4+TRBV6+ T cells from XPR1 cKO *Marilyn* mice compared to CTL *Marilyn* mice (Fig. 3, F and G), suggesting that XPR1 absence triggered a heightened response of naïve T cells towards antigen-specific stimulation *in vivo*. Using

siRNA-mediated knockdown experiments (Fig. 3H), we found elevated *IL22* and *IFNG* mRNA levels upon XPR1 reduction in Jurkat cells, validating an inhibitory XPR1 effect on cytokine transcription in human cells (Fig. 3I).

XPR1 restricts CD28 costimulation

Indicating a shift in signaling similar to enhanced CD28 costimulation [23,24], we investigated whether XPR1-deficient T cells have an increased sensitivity towards CD28 stimulation. In addition to increased proliferation of CD4+ T cells from XPR1 cKO compared to CTL mice stimulated with high anti-CD3/anti-CD28 concentrations, a proliferative response of XPR1-deficient CD4+ T cells was already induced by stimulation with low concentrations of anti-CD28 alone (Fig. 4A). Consistently, the proliferative advantage of XPR1-deficient T cells persisted under conditions with suboptimal anti-CD3 stimulation, whereas no proliferation above baseline levels was detectable for T cells with normal XPR1 expression. To address membrane rearrangement as a potential mechanism for differential CD28 costimulation by XPR1 deficiency [25], we performed imaging flow cytometry and CD28 kinetic analyses. Stimulated CD4+ T cells from XPR1 cKO mice displayed enhanced clustering of their stained cytoplasmic membrane than CD4+ T cells from CTL littermates, which was made evident by an increased average spot number per cell (Fig. 4B and Fig. S11A). Moreover, labelling and subsequent cross-linking revealed an accumulated detection of CD28 on the surface over time, which achieved higher levels in XPR1-deficient CD4+ T cells compared to controls (Fig. 4C). To further demonstrate that increased proliferation of XPR1-deficient CD4+ T cells depends on CD28 costimulation, we compared CD28-independent homeostatic expansion of naïve CD4+ T cells with or without XPR1 expression after adoptive transfer into lymphopenic *Rag2*$^{-/-}$ mice [26]. In contrast to TCR/CD28-mediated stimulation of antigen-specific T cells (Fig. 3E), the proliferative advantage of XPR1-deficient CD4+ T cells was abrogated in the context of CD28-independent homeostatic expansion (Fig. 4D). Further validating the role of costimulation for hyperproliferative responses of T cells lacking XPR1 expression, clonal expansion of female CD4+ T cells from XPR1 cKO *Marilyn* showed less proliferation compared to CTL *Marilyn* mice when competing for non-activated APC from male splenocytes (Fig. S11B). XPR1 deficiency, however, moderately increased T-cell activation in co-culture experiments with irradiated APCs (Fig. S11C). Furthermore, in response to PMA/ionomycin and staphylococcal enterotoxin B stimulation, CD4+ T cells with or without XPR1 expression proliferated similarly, suggesting that XPR1 deficiency does not impact T-cell proliferation when receptor-mediated signaling is bypassed or excessively activated, respectively (Fig. S11, D and E).

XPR1-KIDINS220 interaction regulates CD28 costimulation through endocytosis

In cancer cells, XPR1 has been recently found to bind KIDINS220 [27,28], an adapter protein that has been shown to regulate signaling processes in neuronal and immune cells [29-32]. We therefore assessed the interaction of XPR1 and KIDINS220 in T cells using proximity ligation assays. Labelling both XPR1 and KIDINS220 with specific antibodies, but not in combination with respective control IgGs, resulted in elevated amplification spot numbers (Fig. 4E), indicating the association of XPR1 with KIDINS220 in CD4+ T cells. To determine the role of XPR1-mediated complex formation for costimulation and

hyperproliferation, we performed protein transduction with membrane-permeable peptides Tat-XPR1-Cterm and Tat-KIDINS220-Clvg that inhibit C-terminal XPR1 binding/trafficking [33,34] and proteolytic cleavage of KIDINS220 [35], respectively (Fig. 5A). As expected, binding competition with endogenous XPR1 led to diminished KIDINS220 association upon Tat-XPR1-Cterm treatment, whereas interfering with endogenous KIDINS220 degradation led to increased association with XPR1 upon Tat-KIDINS220-Clvg treatment (Fig. 5B). Consistent with enhanced CD28 detection in XPR1-deficient CD4+ T cells, the surplus of the C-terminal XPR1 binding site through Tat-XPR1-Cterm transfer also increased CD28 surface clustering (Fig. 5C). Intriguingly, this effect also occurred by KIDINS220 stabilization through Tat-KIDINS220-Clvg transfer, indicating that increased availability of KIDINS220 may enhance, whereas its association with XPR1 may restrict CD28 costimulation. This is in line with our results in CD4+ T cells from XPR1 cKO mice, where enhanced CD28 surface clustering did not further increase upon Tat-XPR1-Cterm or Tat-KIDINS220-Clvg treatment. To test whether impediment of the XPR1 association with KIDINS220 leads to hyperproliferation in CD4+ T cells, we treated CD4+ T cells with Tat-XPR1-Cterm and Tat-KIDINS220-Clvg before stimulation with anti-CD3/anti-CD28 *in vitro*. In addition to enhanced CD28 surface clustering, interfering with the XPR1-KIDINS220 interaction increased proliferation in CD4+ T cells from XPR1 CTL mice, but did not further increase proliferation in CD4+ T cells from XPR1 cKO mice (Fig. 5D). Furthermore, RNA-seq analysis revealed a similarity of transcriptional changes between Tat-XPR1-Cterm and Tat-KIDINS220-Clvg treated CD4+ T cells from CTL mice in comparison to vehicle control treatment (Fig. S12A). In total, an overlap of 4826 differentially expressed genes (DEGs) were up- or down-regulated (2300 vs. 2526 DEGs) upon Tat-XPR1-Cterm or Tat-KIDINS220-Clvg transfer (Fig. 5E and Fig. S12B), that are related to pathways including endocytosis and plasma membrane interactions (Fig. S12C), involved in protein binding and neuronal and immunological diseases (Fig. S12D). Gene set enrichment analyses recognized transcriptional signatures for endocytosis (GO_term: 04144) as target program for both the inhibition of C-terminal XPR1 binding/trafficking mediated by Tat-XPR1-Cterm transfer and the inhibition of KIDINS220 degradation mediated by Tat-KIDINS220-Clvg transfer (Fig. 5E), suggesting that altered endocytosis by interference with the XPR1-KIDINS220 interaction induces CD28 costimulation-driven hyperproliferation.

Since the C-terminal protein sequence of murine XPR1 and human XPR1 is identical, we tested whether protein transduction with Tat-XPR1-Cterm could also impact on CD28 costimulation in human T cells. In comparison to buffer controls, Tat-XPR1-Cterm treatment increased CD28 surface clustering and IL-17A expression in stimulated CD4+ T cells isolated from PBMCs of healthy donors (Fig. 5F), indicating that XPR1 protein binding properties are a potential target to enhance CD4+ T-cell responses.

In summary, XPR1 emerges as adapter protein that interferes with CD28 costimulation by sequestering KIDINS220, as XPR1 deficiency results in elevated AKT/mTOR-mediated cytokine expression and hyperproliferation of CD4+ T cells.

DISCUSSION

XPR1 was originally described as entry receptor for murine leukemia retroviruses [36] and later identified as phosphate exporter that provides cellular phosphate homeostasis in various cell types [37]. Recently, the dimeric structure of XPR1 has been resolved and regulation of the phosphate channel activity via inositol pyrophosphate (1,5-InsP8) binding to the SYG1/PHO/XPR1 (SPX) domain has been demonstrated [15,34,16]. In addition to phosphate export, XPR1 also controls phosphate import through interaction with solute carrier protein SLC20A1/PiT1 [14], indicating that XPR1 mutations found in PFBC patients may have implications beyond phosphate transport defects [38]. Intriguingly, another phosphate exporter has been reported in yeast [39], suggesting that compensatory mechanisms maintain phosphate homeostasis in XPR1-deficient CD4+ T cells.

We found that *Xpr1* gene deletion in CD4+ T cells diminishes Ca^{2+} mobilization from intracellular Ca^{2+} stores and extracellular Ca^{2+} entry as well as subsequent ERK/NFAT signaling. Similarly, decreased Ca^{2+} fluxes have been reported in B cells and astrocytes with KIDINS220 deficiency [40,41], pointing towards a cooperative role of both membrane proteins for Ca^{2+} signaling. XPR1 and KIDINS220 have a PDZ-binding motif that facilitates trafficking as cargo of sortin nexin 27 [42,33]. The PDZ-binding motif of XPR1 is located at the C-terminal region of XPR1, which has been shown to be important for protein localization and/or stability [43,44]. Thus, the transfer of Tat-XPR1_Cterm into CD4+ T cells may block interaction partners and/or increase proteasomal degradation of XPR1. Either way, our finding that the hyperproliferative phenotype of XPR1-deficient CD4+ T cells is mirrored by Tat-XPR1_Cterm as well as Tat-KIDINS220-Clvg treatment, underscores the relevance of the XPR1-KIDINS220 association for T-cell responses. Mechanistically, binding competition for XPR1 and stabilization of KIDINS220, mediated by respective membrane-permeable peptide transfer, affects endocytosis in CD4+ T cells. This is in line with a recent report that XPR1 deficiency leads to impaired fetal liver macrophage differentiation in combination with a reduced ability to clear nuclei expelled from erythroblasts [5].

In XPR1 cKO mice, thymocyte development was impaired and peripheral CD4+ T cells expressed more IL-2 and pro-inflammatory cytokines – changes related to dysregulated CD28 signaling [45,46]. Consistently, we observed elevated AKT/mTOR pathway activation and aberrant membrane rearrangement with enhanced CD28 surface clustering in CD4+ T cells lacking XPR1. Moreover, hyperresponsiveness to anti-CD28 stimulation triggered proliferation in murine XPR1-deficient CD4+ T cells and promoted IL-17A expression in human CD4+ T cells treated with Tat-XPR1_Cterm, indicative for strong CD28 signaling [47,48]. Thus, XPR1 emerges as rheostat for CD28 costimulation and as potential target for immunomodulation [49].

Further investigations will have to clarify, whether membrane receptors other than CD28 are also affected by impaired endocytosis and whether signaling pathways also depend intrinsically on XPR1 as adapter protein or predominantly rely on endocytosis regulation through the XPR1-KIDINS220 axis. In summary, we found XPR1 deficiency induces hyperactivation and elevated cytokine expression

and identified XPR1 as novel target for immunomodulation of CD4+ T cells.

MATERIALS AND METHODS

Animals

Mice strains were bred in-house on a C57BL/6J background and cells from thymus, spleen and mesenteric lymph nodes were analyzed that originated from wild type mice, *Rag2*$^{-/-}$ mice (Rag2^{tm1Fwa}; RRID:NSRRC_0035) and cross-breeds of XPR1-floxed (C57BL/6-*Xpr1*$^{tm1.1Frsv}$/J; RRID:IMSR_JAX:037220) and CD4-Cre driver mice (B6.Cg-Tg(Cd4-cre)1Cwi/BfluJ; RRID:IMSR_JAX:#017336), to generate conditional XPR1 knockout mice (cKO, *Cd4-Cre*$^{+}$ *Xpr1*$^{fl/fl}$) in comparison to conditional heterozygous (cHET, *Cd4-Cre*$^{+}$ *Xpr1*$^{wt/fl}$) and (CTL, *Xpr1*$^{fl/fl}$) littermates, as well as cross-breeds of XPR1 cKO and CTL mice with TCR-transgenic *Marilyn* mice (B6.Cg-Ptprc^{a} Rag2^{tm1Fwa} Tg(TcraH-Y,TcrbH-Y)1Pas/PasOrl; RRID:IMSR_EM:00133), to generate *Marilyn* mice with or without T cell-specific deficiency for XPR1 (XPR1 cKO *Marilyn* and CTL *Marilyn* mice). Mice were kept in specific pathogen-free conditions in ventilated cages under standard care protocol with 1320P (Altromin) diet. Intravenuous injections of male H-Y antigen (10 mg/kg body weight; oligopeptide sequence: NAGFNSNRANSSRSS [50], ThermoFisher) into female XPR1 cKO and CTL *Marilyn* mice was performed to analyze activation/differentiation status of antigen-specific TRBV6+CD4+ T cells with or without XPR1 expression from mesenteric lymph nodes after 6 days *in vivo*. For adoptive transfers, 1x10^{6} naïve CD4+ T cells each isolated from XPR1 cKO and CTL mice, labelled with either eFluor450 or eFluor670 proliferation dye and mixed in a 1:1 ratio were intravenously injected into lymphopenic *Rag2*$^{-/-}$ mice to compare XPR1-dependent homeostatic expansion *in vivo*. This study was carried out in accordance with the recommendations of Directive 2010/63/EU of the European Parliament on the protection of animals used for scientific purposes. The protocol was approved by the Behörde für Justiz und Verbraucherschutz der Freien und Hansestadt Hamburg (permit numbers: Org1099; N086/22, N024/16).

Cells

Using histopaque (Sigma) for density gradient centrifugation, PBMCs were prepared from buffy coats obtained from healthy blood donors. Naive human CD4+ T cells were isolated from PBMCs using human naïve CD4+ T cell Isolation Kit II (Miltenyi) and incubated with 3 µM Tat-XPR1_Cterm (oligopeptide sequence: YGRKKRRQRRRPRLASQSKARDTKVLIEDTDDEANT, GeneScript) or DMSO control treatment for 90 min in serum-free X-Vivo medium (Lonza). Following two washing steps, human T cells were stimulated with 5 µg/ml plate-bound anti-CD3 (clone: UCHT1) and 0.5 µg/ml anti-CD28 (clone: 28.2) and cultured for four days.

Jurkat cells (ATCC #TIB-152) were cultured in RPMI 1640 +GlutaMax supplemented with 10% FCS and 1% penicillin/streptomycin. Transfections with siRNA (siXPR1; ThermoFisher, s17614 cat. #4392420) or

scrambled siRNA (cat. #4390843) were performed twice on consecutive days using Lipofectamine RNAiMAX (ThermoFisher) and analyzed after four days.

Primary mouse CD4+ T cells were cultured in RPMI 1640 +GlutaMax supplemented with 10 % FCS, 10 mM HEPES, 1 mM pyruvate, 50 µM β-mercaptoethanol, 1% MEM NEAA, 1% L-glutamine and 1% penicillin/streptomycin. T-cell populations were isolated by magnetic separation using Naïve CD4+ T Cell Isolation kit, CD4+ T Cell Isolation Kit and MicroBeads for isolation of PE- or biotin-labelled CD4+ T cells (Miltenyi Biotec). *In-vitro* stimulation of CD4+ T cells was performed for three days with 5 µg/ml plate-bound anti-CD3 (clone: 145-2C11) and 1 µg/ml soluble anti-CD28 (clone: 37.51), unless stated otherwise. Some conditions used 50 ng/ml phorbol 12-myristate 13-acetate (PMA) and 1 µg/ml ionomycin or 1 µg/ml streptococcal enterotoxin B (SEB, Sigma) for CD28-independent stimulation, while in other experiments 5 µg/ml plate-bound anti-CD3 were used in combination with irradiated APCs (30 Gy, 1:2 ratio) instead of anti-CD28 or untreated whole splenocytes were used for antigen presentation (1:2 ratio) of TCR-transgenic CD4+ T cells. Cell proliferation was assessed by dilution of proliferation dyes (eFluor450, eFluor670 or carboxyfluorescein succinimidyl ester, all ThermoFisher).

Polarization of naive CD4+ T cells was performed with 2 µg/ml anti-CD3 and 0.5 µg/ml anti-CD28 stimulation for three days, except for Th17 cells cultures (5 µg/ml anti-CD3 for five days). Skewing conditions for Th0 cells (1 µg/ml IL-2), Th1 cells (1 µg/ml IL-2, 5 ng/ml IL-12, 10 µg/ml anti-IL-4), Th2 cells (1 µg/ml IL-2, 4 ng/ml IL-4, 10 µg/ml anti-IFN-g), iTreg cells (2 µg/ml IL-2, 10 ng/ml TGF-b, 1 µg/ml anti-IL-4, 1 µg/ml anti-IFN-g) and Th17 cells (1 ng/ml TGF-b, 50 ng/ml IL-6, 5 ng/ml IL-23, 10 µg/ml anti-IL-4, 10 µg/ml anti-IFN-g, 5 µg/ml anti-CD28 or CellXVivo Mouse Th17 Cell Differentiation Kit (R&D Systems) were used.

Transfer of membrane-permeable peptides (according to NP_004727.2 and NP_035403.1 for human/mouse XPR1 and NP_001074847.1 for murine KIDINS220, respectively) into murine CD4+ T cells was performed by 90 min incubation with 3 µM synthetic Tat-XPR1_Cterm and Tat-KIDINS220-Clvg (GeneScript; oligopeptide sequences: YGRKKRRQRRRPRLASQSKARDTKVLIEDTDDEANT and YGRKKRRQRRRPPLNRTPSTVTLNNNT, respectively) or DMSO vehicle control. Following protein transduction, cells were washed twice before further analyses were performed.

Flow cytometric analysis

Flow cytometry was performed on cells within the lymphocyte gate of forward/side scatter plots, excluding doublets and dead cells (LIVE/DEAD Fixable Aqua Dead Cell Stain Kit; ThermoFisher) gated on living CD4+ T-cell populations. Fc receptor binding was prevented (Human BD Fc block and anti-CD16/CD32 blockade, respectively; BD Biosciences) and unspecific binding was excluded by isotype control stainings (BD Biosciences). Intracellular staining of cytokines was performed on cells restimulated with 50 ng/ml PMA and 1 µg/ml ionomycin for six hours, supplemented with GolgiPlug (BD Biosciences) for the last four hours before fixation/permeabilization using FOXP3/Transcription Factor

Staining Buffer Set (ThermoFisher). Fluorescently-labelled antibody clones against human proteins were purchased from BioLegend and ThermoFisher: anti-CD4 (RPA-T4), anti-CD28 (CD28.2) and anti-IL-17A (ebio64DEC17). Fluorescently-labelled antibody clones against murine proteins were purchased from BioLegend, Miltenyi, BD Biosciences or ThermoFisher: anti-CD4 (GK1.5), anti-CD5 (53-7.3), anti-CD8 (53-6.7), anti-CD25 (PC61), anti-CD44 (IM7), anti-CD62L (MEL-14), anti-CD69 (H1.2F3), anti-CD71 (R17217), anti-TCRb (H57-597), anti-Ki-67 (REA183), anti-PD-1 (J43), anti-CTLA-4 (UC10-4B9), anti-TNF-a (MP6-XT22), anti-IFN-g (XMG1.2), anti-IL-4 (11B11), anti-IL-17a (TC11-18H10), anti-IL-22 (Poly5164), anti-FOXP3 (FJK-16s), anti-T-bet (4B10), anti-GATA3 (16E10A23) and anti-RORgt (Q31-378). For comparison of CD28 surface clustering, equal amounts of XPR1 cKO and CTL CD4+ T cells were analyzed by 2 min data acquisition, labelling with hamster anti-mouse CD28 PE-Cy7 (37.51, BioLegend, 0.6 mg/ml) for 8 min and goat anti-hamster crosslinking IgG (Abcam; 5 mg/ml) for 20 min. Flow cytometric analysis was performed on Canto II (BD Biosciences) and NovoCyte Quanteon (Agilent Technologies) instruments and FlowJo 10.10.0 software (Treestar) was used for analysis.

For nuclear translocation analysis by imaging flow cytometry, cells were stained with anti-CD4-PE (GK1.5, Biolegend), anti-NFAT1-Alexa488 (Cell Signaling Technology) and 4',6-diamidino-2-phenylindole (DAPI, ThermoFisher), while anti-CD4-APC-Cy7 (GK1.5, Biolegend) and CellBrite cytoplasmatic membrane dye green (Biotium, 5 mg/ml) staining was used to analyze spot formation of CD4+ T cells treated with hamster anti-mouse CD3 (145-2C11, 5 mg/ml) and goat anti-hamster crosslinking IgG (Abcam; 5 mg/ml) for 90 min. Imaging flow cytometry was performed on Amnis ImageStreamX MkII (Cytek Biosciences) at 60x magnification and IDEAS v6.2 (Merck) using spot count and similarity score features for analysis.

Gene expression array

Naive CD4+ T cells isolated from XPR1 cKO and CTL mice were stimulated with 5 µg/ml plate-bound anti-CD3 and 1 µg/ml soluble anti-CD28 for 6 h, washed with ice-cold PBS and RNA was isolated using RNeasy Micro kit (Qiagen). Whole transcriptome analysis was performed by Clariom D mouse microarrays (ThermoFisher) according to the manual of GeneChip WT PLUS reagent kit. For each sample 100 ng of RNA was amplified and labelled; 5 µg of fragmented, labelled cDNA per sample were used for the array. Fluidics Station 450 was applied for washing and staining and a GeneChip Scanner 3000 7G (ThermoFisher) was used for scanning. Transcriptome Analysis Console Software TAC 4.0 with default analysis settings (version2) was utilized for data analysis and Gene+Exon-SST-RMA for summarisation. Publicly available software program GREAT v4.0.4 was used for pathway prediction analysis.

Ca^{2+} mobilization

Time-lapse microscopy was performed with ratiometric Ca^{2+} reporter dye Fura2-AM in naive CD4+ T cells isolated from XPR1 cKO and CTL mice treated with 10 µg/ml anti-CD3 at 1 min and 1.67 µM thapsigargin at 11 min measurement time. Live cell imaging was performed with a Leica IRBE

microscope at 40x magnification and exposure of 25 ms, using Volocity v6.6.2 for acquisition. The acquisition frame rate was set to 1 frame every 2 s in 16-bit mode. Two excitation filters (HC 340/26 nm and HC 387/11 nm), one beam splitter (T400 LP) and an emission filter (510/84 nm) were used. Fiji 2v (ImageJ) was used for background correction, splitting of fluorescence channels and selection of cells. To calculate Ca^{2+} concentrations, a calibration was obtained by measuring the maximal ratio value Rmax and the minimal ratio value Rmin. Using this, the mean Ca^{2+} concentration over time and the area under the curve (AUC) were calculated.

Real-time PCR

Using RNeasy mini kit (Qiagen) to isolate mRNA and NanoDrop 1000 Spectrophotometer to determine mRNA concentrations, reverse transcription with SuperScript VILO Master Mix (ThermoFisher) and subsequently real-time PCR with TaqMan Universal Master Mix II (ThermoFisher) and specific TaqMan probes was performed: *XPR1* (Hs00173707_m1), *IFNG* (Hs00989291_m1) and *IL22* (Hs00989291_m1) for human and *Xpr1* (Mm00495501_m1) for murine transcripts. Using StepOnePlus Realtime PCR system (ThermoFisher Scientific) for measurements, data were calculated with $[c]=2^{-\Delta\Delta Ct}$ with normalization to housekeeping gene hypoxanthine-guanine phosphoribosyltransferase (human *HPRT*, Hs02800695_m1 and murine *Hprt1*, Mm00446968_m1, respectively).

Immunoblotting

Cells were washed with PBS and pellets were lysed in RIPA buffer supplemented with Halt Protease and Phosphatase Inhibitor Cocktail (ThermoFisher) for 30 min on ice, sonicated and cleared from insoluble debris by centrifugation at 13,000 *g* for 20 min at 4°C. Protein concentrations were determined using Pierce BCA Protein Assay Kit (ThermoFisher) and equal protein amounts were denatured in Laemmli buffer at 95°C for 5 min before SDS-PAGE. Proteins transferred onto polyvinylidene fluoride membrane were probed for XPR1 using antibodies from Proteintech and Sigma-Aldrich (polyclonal rabbit IgG; cat. #14174-1-AP and monoclonal mouse IgG 2G8; cat. #SAB1402458, respectively). Signaling pathways were assessed by immunoblotting with antibodies from Cell Signaling Biosciences: anti-AKT (11E7), anti-phosho-S473-AKT (D9E) and anti-S6 (5G10), from MyBioSource: anti-phospho-S235/S236-S6 (polyclonal) and BioLegend: anti-ERK1/2 (W15133B), anti-phospho-T202/T204-ERK1/2 (6B8B69) and R&D Systems: anti-b-actin (937215). Following incubation with peroxidase-conjugated secondary antibodies, chemiluminescence was detected using ECL Select Western Blotting Detection Reagent (Amersham) in a ChemiDoc Imager (Bio-Rad). Densitometric analysis was performed using ImageJ 2.1.0 (NIH) software and values were calculated relative to the corresponding band intensity of b-actin.

Enzyme-linked immunosorbent assay

IL-2 in supernatants from murine CD4+ T-cell cultures was measured with ELISA-MAX mouse IL-2 set (BioLegend) according to manufacturer's instructions.

Proximity ligation assay

Isolated CD4+ T cells from CTL mice with or without prior treatment with membrane-permeable oligopeptides were attached to coverslips coated with fibronectin (1:50 in PBS for 1 h at 37 °C), washed with PBS and fixed with 4% PFA/PBS for 15 min at 37 °C, followed by two PBS washing steps. Duolink In Situ PLA reagents (Sigma-Aldrich) were used according to manufacturer's instructions. In brief, sample coverslips were transferred onto individual Duolink Blocking Solution drops in a prewarmed humid chamber for 1 h at 37 °C. Incubation of samples with mouse anti-XPR1 (2G8, Sigma-Aldrich) or mouse IgG1 (P3.6.2.8.1, ThermoFisher) in combination with rabbit anti-KIDINS220 (polyclonal, ThermoFisher) or rabbit IgG (polyclonal, Vectorlabs) was done in Duolink Antibody Diluent overnight at 4 °C. Sample coverslips were washed twice with 1x Wash Buffer A for 5 min followed by incubation with Duolink In Situ PLA Probe Anti-Rabbit PLUS and Duolink In Situ PLA Probe Anti-Mouse MINUS in a prewarmed humid chamber for 1 h at 37°C and two washing steps. Likewise, subsequent incubation with ligase in 1x Duolink Ligation Buffer and washing was performed. Duolink In Situ Detection Reagents Red and polymerase in Duolink 1x Amplification Buffer was applied to sample coverslips and incubated for 100 min at 37 °C. Following two washing steps with 1x Wash Buffer B, microscopy slides were mounted using Duolink In Situ Mounting Medium with DAPI. Confocal microscopy imaging was performed on Olympus Fluoview FV3000 (Evident Europe) using a 60x objective. Analysis was performed using the Cell Counter plugin of ImageJ to quantify interaction spots per cell.

RNA sequencing

Transcriptome sequencing was performed with RNA from naïve CD4+ T cells isolated from XPR1 cKO and CTL mice that were treated with 3 µM Tat-XPR1_Cterm, Tat-KIDINS220-Clvg or DMSO vehicle control and stimulated with 5 µg/ml plate-bound anti-CD3 and 1 µg/ml soluble anti-CD28 for three days. DNBseq PE100 sequencing with 20M reads per sample (BGI Genomics) and subsequent bioinformatic data analysis (Dr. Tom Data Visualisation Solution) was performed.

Negative DAPI staining

T-cell polyphosphate was visualized by negative DAPI staining as previously described [19]. In brief, $1x10^6$ isolated CD4+ T cells per sample were washed twice with 50 mM Tris buffer (pH 7.4) and lysed in 0.5% SDS containing 50 mM Tris buffer (pH 7.4, 10 min at ambient temperature) before subjecting samples to debris precipitation (N3 buffer added to lysate in a seven to ten volume ratio), debris removal (18,000 *g*, 10 min) and DNA column binding (QIAprep Spin Kit extraction columns, Qiagen) according to manufacturer's instructions (QIAprep Spin Miniprep Kit, Qiagen). Polyphosphate from flow-through fractions was isolated by phenol-chloroform extraction by addition of one volume phenol/chloroform/isoamylalcohol solution (Roth) and centrifugation at 10,000 *g* for 5 min. The aqueous phase was combined with supernatants from two washing steps of the organic phase with 20 mM Tris buffer (pH 7.4) before one volume chloroform was added and subsequent centrifugation at 10,000 *g* for 5 min. Polyphosphate was precipitated with 20 mM ammonium sulfate, 0.3 M sodium acetate and one volume of ice-cold ethanol, pelleted (10,000 *g* for 10 min at 4°C) and air-dried overnight. Polyphosphate pellets were dissolved in 50 mM Tris buffer (pH 7.4) and 2x TBE urea sample buffer (ThermoFisher) and

loaded on 8% PAGE gels containing 63% (w/v) urea. Following size separation at 120 V, gels were stained with 2.5 µg/ml DAPI in staining buffer (25% methanol, 5% glycerol, pH 8.0) for 30 min, washed with staining buffer for 1 h and imaging was performed after photobleaching by UV light exposure with a ChemiDoc Imager (Bio-Rad). Negative DAPI staining of 20 ng synthetic polyphosphate (PhosCheck P30, BK Giulini) and a 383-mer polyphosphate standard (kindly provided by Dr. James H. Morrissey, University of Michigan Medical School, USA) was used as reference control and for size comparison.

Malachite green assay

Polyphosphate quantification was performed by colorimetric assays in SDS-free aqueous solutions as previously described [51]. In brief, CD4+ T cells were washed twice with 50 mM Tris buffer (pH 7.4), resuspended (25 mM MOPS, 2.5 mM EDTA, pH 7.0), mixed with phenol-saturated Tris buffer (10 mM Tris, 1 mM EDTA, pH 7.5) in a 4:3 volume ratio and incubated for 10 min at 45°C and another 2 min on ice. After chloroform was added to the phenol containing lysate in a ten to seven volume ratio, samples were rigorously vortexed and centrifuged at 12,000 *g* for 5 min at 4°C. Equal parts of the aqueous phase were either used for polyphosphate hydrolysis (1 M HCl, 95°C, 10 min) with subsequent pH neutralization (1 M NaOH) to obtain values for total phosphate concentrations or volume adjusted to measure phosphate background levels using Phosphate Assay Kit (Colorimetric) (Abcam). Polyphosphate levels were calculated by subtraction of background values from the total phosphate concentration according to manufacturer's instructions.

Statistics

Values are expressed as mean ± SEM; Shapiro-Wilk normality test was performed to assess normal distribution of data sets. Paired and unpaired Student *t* test and non-parametric Mann-Whitney test was used for comparisons of two groups; One-sample *t* test was used for comparison of normalized data; One-Way ANOVA followed by Tukey multiple comparisons test and Kruskal-Wallis ANOVA followed by Dunn multiple comparisons test was performed to compare normal and not normally distributed data from more than two groups, respectively; Two-way ANOVA followed by Sidak multiple comparisons test was performed to compare data from more than two groups with two independent variables, as indicated. Differences were considered significant at $p < 0.05$ (2-tailed); all statistical analyses were performed using GraphPad Prism 8.4.3 software.

Declarations

Supplementary information is available at *Cellular & Molecular Immunology*'s website.

ACKNOWLEGEMENTS

The authors would like to thank Christian Krebs (Hamburg Center for Translational Immunology, Germany) and Dimitri Firsov (University of Lausanne, France) for providing mouse lines. We also thank care takers of the animal facility at the UKE, the Microscopy Imaging Facility at the UKE (DFG Research Infrastructure Portal: RI_00489) and the Cytometry und Cell Sorting Core Unit at the UKE for technical support.

Funding

This work was supported by:

German Research Foundation grant 470698011 (RKM)

German Research Foundation grant 335447717 (SFB1328 project A02) (B-PD)

European Union grant 101281504 (PULSE) (TR).

AUTHOR CONTRIBUTIONS

Conceptualization: RKM

Methodology: MMe, BK, MMa, TAY, B-PD, RKM

Investigation: MMe, BK, MMa, TAY, B-PD, RKM

Visualization: MMe, BK, MMa, TAY, B-PD, RKM

Funding acquisition: RKM

Project administration: RKM

Supervision: RKM

Writing – original draft: RKM

Writing – review & editing: MMe, BK, MF, TR, TAY, B-PD, RKM.

DECLARATION OF INTERESTS

Authors declare that they have no competing interests in relation to the work described.

Data and code availability

Gene expression data are accessible through GEO series accession number GSE338616 (Token: qvexeuucbtqtlih) and RNA sequencing data are accessible through GEO series accession number GSE338835 (Token: axohoymurfclpeh).

References

1. Legati, A., Giovannini, D., Nicolas, G., Lopez-Sanchez, U., Quintans, B., Oliveira, J. R., Sears, R. L., Ramos, E. M., Spiteri, E., Sobrido, M. J., Carracedo, A., Castro-Fernandez, C., Cubizolle, S., Fogel, B. L., Goizet, C., Jen, J. C., Kirdlarp, S., Lang, A. E., Miedzybrodzka, Z., Mitarnun, W., Paucar, M., Paulson, H., Pariente, J., Richard, A. C., Salins, N. S., Simpson, S. A., Striano, P., Svenningsson, P., Tison, F., Unni, V. K., Vanakker, O., Wessels, M. W., Wetchaphanphesat, S., Yang, M., Boller, F., Campion, D., Hannequin, D., Sitbon, M., Geschwind, D. H., Battini, J. L. & Coppola, G. Mutations in XPR1 cause primary familial brain calcification associated with altered phosphate export. *Nat Genet* 47, 579–581, doi:10.1038/ng.3289 (2015).
2. Ansermet, C., Moor, M. B., Centeno, G., Auberson, M., Hu, D. Z., Baron, R., Nikolaeva, S., Haenzi, B., Katanaeva, N., Gautschi, I., Katanaev, V., Rotman, S., Koesters, R., Schild, L., Pradervand, S., Bonny, O. & Firsov, D. Renal Fanconi Syndrome and Hypophosphatemic Rickets in the Absence of Xenotropic and Polytropic Retroviral Receptor in the Nephron. *J Am Soc Nephrol* 28, 1073–1078, doi:10.1681/ASN.2016070726 (2017).
3. Maheshwari, U., Mateos, J. M., Weber-Stadlbauer, U., Ni, R., Tamatey, V., Sridhar, S., Restrepo, A., de Jong, P. A., Huang, S. F., Schaffenrath, J., Stifter, S. A., Szeri, F., Greter, M., Koek, H. L. & Keller, A. Inorganic phosphate exporter heterozygosity in mice leads to brain vascular calcification, microangiopathy, and microgliosis. *Brain Pathol* 33, e13189, doi:10.1111/bpa.13189 (2023).
4. Xu, X., Li, X., Sun, H., Cao, Z., Gao, R., Niu, T., Wang, Y., Ma, T., Chen, R., Wang, C., Yang, Z. & Liu, J. Y. Murine placental-fetal phosphate dyshomeostasis caused by an Xpr1 deficiency accelerates placental calcification and restricts fetal growth in late gestation. *Journal of bone and mineral research: the official journal of the American Society for Bone and Mineral Research*, doi:10.1002/jbmr.3866 (2019).
5. Stifter, S. A., Bijnen, M., Tuzlak, S., Petrova, E., Hane, P., Roussel, E., Van Hove, H., Asano, K., Becher, B., Keller, A. & Greter, M. XPR1 regulates fetal liver macrophage development, identity, and pyrenocyte clearance. *J Exp Med* 223, doi:10.1084/jem.20241587 (2026).
6. Esensten, J. H., Helou, Y. A., Chopra, G., Weiss, A. & Bluestone, J. A. CD28 Costimulation: From Mechanism to Therapy. *Immunity* 44, 973–988, doi:10.1016/j.immuni.2016.04.020 (2016).
7. Delgoffe, G. M., Kole, T. P., Zheng, Y., Zarek, P. E., Matthews, K. L., Xiao, B., Worley, P. F., Kozma, S. C. & Powell, J. D. The mTOR kinase differentially regulates effector and regulatory T cell lineage commitment. *Immunity* 30, 832–844, doi:10.1016/j.immuni.2009.04.014 (2009).
8. Kurebayashi, Y., Nagai, S., Ikejiri, A., Ohtani, M., Ichiyama, K., Baba, Y., Yamada, T., Egami, S., Hoshii, T., Hirao, A., Matsuda, S. & Koyasu, S. PI3K-Akt-mTORC1-S6K1/2 axis controls Th17 differentiation by regulating Gfi1 expression and nuclear translocation of RORgamma. *Cell Rep* 1, 360–373, doi:10.1016/j.celrep.2012.02.007 (2012).
9. Lai, Y., Wang, S., Ren, T., Shi, J., Qian, Y., Wang, S., Zhou, M., Watanabe, R., Li, M., Ruan, X., Wang, X., Zhuang, L., Ke, Z., Yang, N., Huang, Y. & Zhang, H. TIGIT deficiency promotes autoreactive CD4(+) T-

cell responses through a metabolic–epigenetic mechanism in autoimmune myositis. *Nat Commun* 16, 4502, doi:10.1038/s41467-025-59786-z (2025).

10. Suntharalingam, G., Perry, M. R., Ward, S., Brett, S. J., Castello-Cortes, A., Brunner, M. D. & Panoskaltsis, N. Cytokine storm in a phase 1 trial of the anti-CD28 monoclonal antibody TGN1412. *N Engl J Med* 355, 1018–1028, doi:10.1056/NEJMoa063842 (2006).
11. Hui, E., Cheung, J., Zhu, J., Su, X., Taylor, M. J., Wallweber, H. A., Sasmal, D. K., Huang, J., Kim, J. M., Mellman, I. & Vale, R. D. T cell costimulatory receptor CD28 is a primary target for PD-1-mediated inhibition. *Science* 355, 1428–1433, doi:10.1126/science.aaf1292 (2017).
12. Tai, X., Van Laethem, F., Sharpe, A. H. & Singer, A. Induction of autoimmune disease in CTLA-4-/- mice depends on a specific CD28 motif that is required for in vivo costimulation. *Proc Natl Acad Sci U S A* 104, 13756–13761, doi:10.1073/pnas.0706509104 (2007).
13. Burns, D., Berlinguer-Palmini, R. & Werner, A. XPR1: a regulator of cellular phosphate homeostasis rather than a Pi exporter. *Pflugers Arch* 476, 861–869, doi:10.1007/s00424-024-02941-0 (2024).
14. Li, X., Kirkpatrick, R. B., Wang, X., Tucker, C. J., Shukla, A., Jessen, H. J., Wang, H., Shears, S. B. & Gu, C. Homeostatic coordination of cellular phosphate uptake and efflux requires an organelle-based receptor for the inositol pyrophosphate IP8. *Cell Rep* 43, 114316, doi:10.1016/j.celrep.2024.114316 (2024).
15. Lu, Y., Yue, C. X., Zhang, L., Yao, D., Xia, Y., Zhang, Q., Zhang, X., Li, S., Shen, Y., Cao, M., Guo, C. R., Qin, A., Zhao, J., Zhou, L., Yu, Y. & Cao, Y. Structural basis for inositol pyrophosphate gating of the phosphate channel XPR1. *Science* 386, eadp3252, doi:10.1126/science.adp3252 (2024).
16. Yan, R., Chen, H., Liu, C., Zhao, J., Wu, D., Jiang, J., Gong, J. & Jiang, D. Human XPR1 structures reveal phosphate export mechanism. *Nature* 633, 960–967, doi:10.1038/s41586-024-07852-9 (2024).
17. Azzam, H. S., Grinberg, A., Lui, K., Shen, H., Shores, E. W. & Love, P. E. CD5 expression is developmentally regulated by T cell receptor (TCR) signals and TCR avidity. *J Exp Med* 188, 2301–2311, doi:10.1084/jem.188.12.2301 (1998).
18. Yamashita, I., Nagata, T., Tada, T. & Nakayama, T. CD69 cell surface expression identifies developing thymocytes which audition for T cell antigen receptor-mediated positive selection. *Int Immunol* 5, 1139–1150, doi:10.1093/intimm/5.9.1139 (1993).
19. Mailer, R. K., Allende, M., Heestermans, M., Schweizer, M., Deppermann, C., Frye, M., Pula, G., Odeberg, J., Gelderblom, M., Rose-John, S., Sickmann, A., Blankenberg, S., Huber, T. B., Kubisch, C., Maas, C., Gambaryan, S., Firsov, D., Stavrou, E. X., Butler, L. M. & Renne, T. Xenotropic and polytropic retrovirus receptor 1 regulates procoagulant platelet polyphosphate. *Blood* 137, 1392–1405, doi:10.1182/blood.2019004617 (2021).
20. Jurgens, A. P., Zwijnen, J., Bradaric, A., van Alphen, F. P. J., Bresser, K., Rooijers, K., Hoogendijk, A. J., Popovic, B. & Wolkers, M. C. mTOR signaling during T cell activation promotes cytokine production in T cells through 3' UTR-mediated translation control. *Mol Cell* 85, 4452–4462 e4455, doi:10.1016/j.molcel.2025.11.005 (2025).

21. Patel, C. H. & Powell, J. D. More TOR: The expanding role of mTOR in regulating immune responses. *Immunity* 58, 1629–1645, doi:10.1016/j.immuni.2025.06.010 (2025).
22. Perez-Diez, A., Joncker, N. T., Choi, K., Chan, W. F., Anderson, C. C., Lantz, O. & Matzinger, P. CD4 cells can be more efficient at tumor rejection than CD8 cells. *Blood* 109, 5346–5354, doi:10.1182/blood-2006-10-051318 (2007).
23. June, C. H., Ledbetter, J. A., Gillespie, M. M., Lindsten, T. & Thompson, C. B. T-cell proliferation involving the CD28 pathway is associated with cyclosporine-resistant interleukin 2 gene expression. *Mol Cell Biol* 7, 4472–4481, doi:10.1128/mcb.7.12.4472-4481.1987 (1987).
24. Kane, L. P., Andres, P. G., Howland, K. C., Abbas, A. K. & Weiss, A. Akt provides the CD28 costimulatory signal for up-regulation of IL-2 and IFN-gamma but not TH2 cytokines. *Nat Immunol* 2, 37–44, doi:10.1038/83144 (2001).
25. Yokosuka, T., Kobayashi, W., Sakata-Sogawa, K., Takamatsu, M., Hashimoto-Tane, A., Dustin, M. L., Tokunaga, M. & Saito, T. Spatiotemporal regulation of T cell costimulation by TCR-CD28 microclusters and protein kinase C theta translocation. *Immunity* 29, 589–601, doi:10.1016/j.immuni.2008.08.011 (2008).
26. Prlic, M., Blazar, B. R., Khoruts, A., Zell, T. & Jameson, S. C. Homeostatic expansion occurs independently of costimulatory signals. *J Immunol* 167, 5664–5668, doi:10.4049/jimmunol.167.10.5664 (2001).
27. Bondeson, D. P., Paolella, B. R., Asfaw, A., Rothberg, M. V., Skipper, T. A., Langan, C., Mesa, G., Gonzalez, A., Surface, L. E., Ito, K., Kazachkova, M., Colgan, W. N., Warren, A., Dempster, J. M., Krill-Burger, J. M., Ericsson, M., Tang, A. A., Fung, I., Chambers, E. S., Abdusamad, M., Dumont, N., Doench, J. G., Piccioni, F., Root, D. E., Boehm, J., Hahn, W. C., Mannstadt, M., McFarland, J. M., Vazquez, F. & Golub, T. R. Phosphate dysregulation via the XPR1-KIDINS220 protein complex is a therapeutic vulnerability in ovarian cancer. *Nat Cancer* 3, 681–695, doi:10.1038/s43018-022-00360-7 (2022).
28. Zuo, P., Wang, W., Dai, Z., Zheng, J., Yu, S., Wang, G., Yin, Y., Liang, L. & Yin, Y. Synergistic activation of the human phosphate exporter XPR1 by KIDINS220 and inositol pyrophosphate. *Nat Commun* 16, 2879, doi:10.1038/s41467-025-58200-y (2025).
29. Deswal, S., Meyer, A., Fiala, G. J., Eisenhardt, A. E., Schmitt, L. C., Salek, M., Brummer, T., Acuto, O. & Schamel, W. W. Kidins220/ARMS associates with B-Raf and the TCR, promoting sustained Erk signaling in T cells. *J Immunol* 190, 1927–1935, doi:10.4049/jimmunol.1200653 (2013).
30. Herr, L. A., Fiala, G. J., Sagar, Schaffer, A. M., Hummel, J. F., Zintchenko, M., Raute, K., Velasco Cardenas, R. M., Heizmann, B., Ebert, K., Fehrenbach, K., Janowska, I., Chan, S., Tanriver, Y., Minguet, S. & Schamel, W. W. Kidins220 and Aiolos promote thymic iNKT cell development by reducing TCR signals. *Sci Adv* 10, eadj2802, doi:10.1126/sciadv.adj2802 (2024).
31. Jean-Mairet, R. M., Lopez-Menendez, C., Sanchez-Ruiloba, L., Sacristan, S., Rodriguez-Martinez, M., Riol-Blanco, L., Sanchez-Mateos, P., Sanchez-Madrid, F., Rodriguez-Fernandez, J. L., Campanero, M. R. & Iglesias, T. The neuronal protein Kidins220/ARMS associates with ICAM-3 and other uropod

components and regulates T-cell motility. *Eur J Immunol* 41, 1035–1046, doi:10.1002/eji.201040513 (2011).

32. Neubrand, V. E., Cesca, F., Benfenati, F. & Schiavo, G. Kidins220/ARMS as a functional mediator of multiple receptor signalling pathways. *J Cell Sci* 125, 1845–1854, doi:10.1242/jcs.102764 (2012).
33. Tello-Lafoz, M., Martinez-Martinez, G., Rodriguez-Rodriguez, C., Albar, J. P., Huse, M., Gharbi, S. & Merida, I. Sorting nexin 27 interactome in T-lymphocytes identifies zona occludens-2 dynamic redistribution at the immune synapse. *Traffic* 18, 491–504, doi:10.1111/tra.12492 (2017).
34. Wang, X., Bai, Z., Wallis, C., Wang, H., Han, Y., Jin, R., Lei, M., Yang, T., Gu, C., Jessen, H., Shears, S., Sun, Y., Corry, B. & Zhang, Y. KIDINS220 and InsP8 safeguard the stepwise regulation of phosphate exporter XPR1. *Mol Cell* 85, 3209–3224 e3208, doi:10.1016/j.molcel.2025.08.003 (2025).
35. Gamir-Morralla, A., Lopez-Menendez, C., Ayuso-Dolado, S., Tejeda, G. S., Montaner, J., Rosell, A., Iglesias, T. & Diaz-Guerra, M. Development of a neuroprotective peptide that preserves survival pathways by preventing Kidins220/ARMS calpain processing induced by excitotoxicity. *Cell Death Dis* 6, e1939, doi:10.1038/cddis.2015.307 (2015).
36. Kozak, C. A. The mouse "xenotropic" gammaretroviruses and their XPR1 receptor. *Retrovirology* 7, 101, doi:10.1186/1742-4690-7-101 (2010).
37. Jennings, M. L. Role of transporters in regulating mammalian intracellular inorganic phosphate. *Front Pharmacol* 14, 1163442, doi:10.3389/fphar.2023.1163442 (2023).
38. Bondeson, D. P. Insights into phosphate homeostasis regulation by XPR1. *Nat Struct Mol Biol* 32, 5–7, doi:10.1038/s41594-024-01460-x (2025).
39. Komamura, T., Nishimura, T., Ohta, N., Takado, M., Matsumoto, T. & Takeda, K. The putative polyamine transporter Shp2 facilitates phosphate export in an Xpr1-independent manner and contributes to high phosphate tolerance. *J Biol Chem* 301, 108056, doi:10.1016/j.jbc.2024.108056 (2025).
40. Fiala, G. J., Janowska, I., Prutek, F., Hobeika, E., Satapathy, A., Sprenger, A., Plum, T., Seidl, M., Dengjel, J., Reth, M., Cesca, F., Brummer, T., Minguet, S. & Schamel, W. W. Kidins220/ARMS binds to the B cell antigen receptor and regulates B cell development and activation. *J Exp Med* 212, 1693–1708, doi:10.1084/jem.20141271 (2015).
41. Jaudon, F., Chiacchiaretta, M., Albini, M., Ferroni, S., Benfenati, F. & Cesca, F. Kidins220/ARMS controls astrocyte calcium signaling and neuron-astrocyte communication. *Cell Death Differ* 27, 1505–1519, doi:10.1038/s41418-019-0431-5 (2020).
42. Steinberg, F., Gallon, M., Winfield, M., Thomas, E. C., Bell, A. J., Heesom, K. J., Tavare, J. M. & Cullen, P. J. A global analysis of SNX27-retromer assembly and cargo specificity reveals a function in glucose and metal ion transport. *Nat Cell Biol* 15, 461–471, doi:10.1038/ncb2721 (2013).
43. Lopez-Sanchez, U., Nicolas, G., Richard, A. C., Maltete, D., Charif, M., Ayrignac, X., Goizet, C., Touhami, J., Labesse, G., Battini, J. L. & Sitbon, M. Characterization of XPR1/SLC53A1 variants located outside of the SPX domain in patients with primary familial brain calcification. *Sci Rep* 9, 6776, doi:10.1038/s41598-019-43255-x (2019).

44. Zhu, Q., Yaggi, M. F., Jork, N., Jessen, H. J. & Diver, M. M. Transport and InsP(8) gating mechanisms of the human inorganic phosphate exporter XPR1. *Nat Commun* 16, 2770, doi:10.1038/s41467-025-58076-y (2025).
45. Raab, M., Pfister, S. & Rudd, C. E. CD28 signaling via VAV/SLP-76 adaptors: regulation of cytokine transcription independent of TCR ligation. *Immunity* 15, 921–933, doi:10.1016/s1074-7613(01)00248-5 (2001).
46. Turner, M., Mee, P. J., Walters, A. E., Quinn, M. E., Mellor, A. L., Zamoyska, R. & Tybulewicz, V. L. A requirement for the Rho-family GTP exchange factor Vav in positive and negative selection of thymocytes. *Immunity* 7, 451–460, doi:10.1016/s1074-7613(00)80367-2 (1997).
47. Tacke, M., Hanke, G., Hanke, T. & Hunig, T. CD28-mediated induction of proliferation in resting T cells in vitro and in vivo without engagement of the T cell receptor: evidence for functionally distinct forms of CD28. *Eur J Immunol* 27, 239–247, doi:10.1002/eji.1830270136 (1997).
48. Thompson, C. B., Lindsten, T., Ledbetter, J. A., Kunkel, S. L., Young, H. A., Emerson, S. G., Leiden, J. M. & June, C. H. CD28 activation pathway regulates the production of multiple T-cell-derived lymphokines/cytokines. *Proc Natl Acad Sci U S A* 86, 1333–1337, doi:10.1073/pnas.86.4.1333 (1989).
49. Lotze, M. T., Olejniczak, S. H. & Skokos, D. CD28 co-stimulation: novel insights and applications in cancer immunotherapy. *Nat Rev Immunol* 24, 878–895, doi:10.1038/s41577-024-01061-1 (2024).
50. Lantz, O., Grandjean, I., Matzinger, P. & Di Santo, J. P. Gamma chain required for naive CD4 + T cell survival but not for antigen proliferation. *Nat Immunol* 1, 54–58, doi:10.1038/76917 (2000).
51. Christ, J. J. & Blank, L. M. Analytical polyphosphate extraction from Saccharomyces cerevisiae. *Anal Biochem* 563, 71–78, doi:10.1016/j.ab.2018.09.021 (2018).

Figures

Figure 1

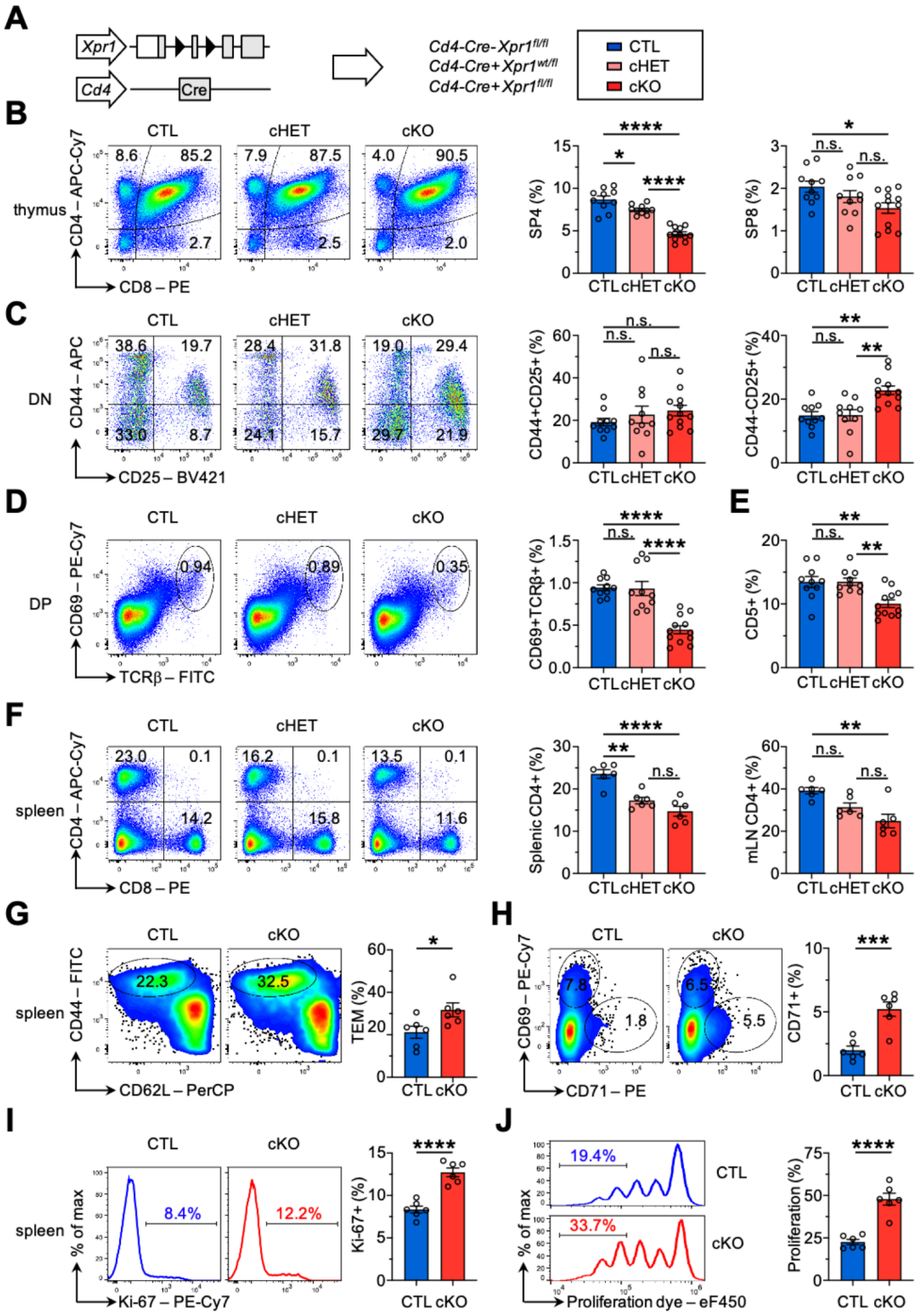


Figure 1

T cell-specific deletion of *Xpr1*impairs thymic development and XPR1-deficient CD4+ T cells are hyperactivated.

(**A**) Schematic overview of T cell-specific *Xpr1* genetic deletion. Resulting murine genotypes with preserved XPR1 expression (CTL, blue) and with XPR1-deficient T cells in one (cHET, light red) or two

alleles (cKO, red).

(**B**) Representative flow cytometry plots (left) and quantification in bar graphs (right) of single positive CD4+ (SP4) and CD8+ (SP8) thymocyte populations; *n*=10,10,12.

(**C**) Representative flow cytometry plots (left) and quantification in bar graphs (right) of double negative (DN) thymocytes with CD44+CD25+ DN stage2 and CD44-CD25+ DN stage3 expression profiles; *n*=10,10,12.

(**D**) Representative flow cytometry plots (left) and quantification in bar graphs (right) of double positive (DP) thymocytes with CD69+TCRβ+ recently selected expression profile; *n*=10,10,12.

(**E**) Quantification of CD5+ populations among DP thymocytes; *n*=10,10,12.

(**F**) Representative flow cytometry plots (left) and quantification in bar graphs (right) of CD4+ T-cell populations in spleen and mesenteric lymph nodes; *n*=6.

(**G**) Representative flow cytometry plots and quantification of CD62L-CD44+ effector memory T-cell populations (TEM) among splenic CD4+ T cells; *n*=6.

(**H**) Representative flow cytometry plots and quantification of CD71+ populations among splenic CD4+ T cells; *n*=6.

(**I**) Representative flow cytometry histograms and quantification of Ki-67+ populations among splenic CD4+ T cells; *n*=6.

(**J**) Representative flow cytometry histograms and quantification of highly proliferating cells after anti-CD3/anti-CD28 stimulation of naïve CD4+ T cells isolated from XPR1 cKO and CTL mice for 72 h; *n*=6.

Values are expressed as mean ± SEM; statistical significance is indicated as $*p < 0.05$, $**p < 0.01$, $***p < 0.001$, $****p < 0.0001$; not significant (n.s.). One-way ANOVA followed by Tukey multiple comparisons test (B-F) and unpaired Student *t*test (G-J) was performed for statistical analysis.

Figure 2

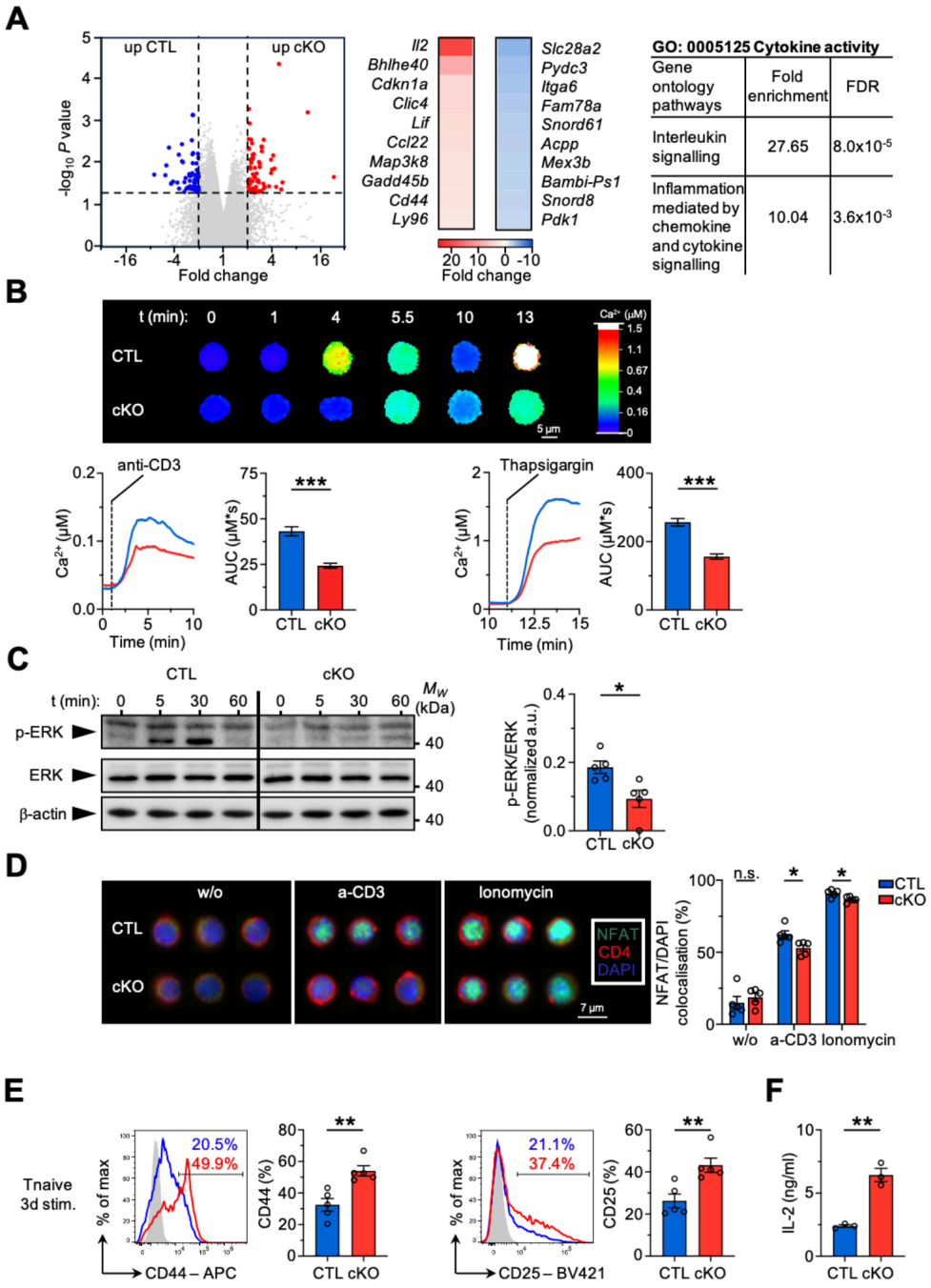


Figure 2

***Xpr1* deletion increases IL-2 independently of Ca^{2+}/ERK signaling in CD4+ T cells.**

(**A**) Gene expression profiling of naïve CD4+ T cells from XPR1 cKO and CTL mice after anti-CD3/anti-CD28 stimulation for 6 h. Volcano plot, top hits of differentially up- and down-regulated genes and gene ontology (GO) pathway analysis from *n*=3 independent experiments is shown.

(**B**) Live cell imaging of naïve CD4+ T cells from XPR1 cKO and CTL mice stimulated with 10 µg/ml anti-CD3 after 1 min, and 1.67 µM thapsigargin after 11 min measurement. Representative single-cell images of intracellular Ca^{2+} fluxes over time, average responses to stimuli and area under the curve (AUC) from *n*=3 independent time-lapse microscopy experiments are shown.

(**C**) Phosphorylation of ERK (p-ERK) in naïve CD4+ T cells from XPR1 cKO and CTL mice after stimulation with 5 µg/ml anti-CD3 for indicated time; quantification of normalized p-ERK/ERK ratio after 5 min stimulation from *n*=5 independent experiments is shown.

(**D**) NFAT nuclear translocation measured by imaging flow cytometry of isolated CD4+ T cells from XPR1 cKO and CTL mice. Representative single cell images of CD4-labelled T cells stained intracellularly for NFAT1 and DAPI after treatment without (w/o) or with 5 µg/ml anti-CD3 (a-CD3) or with 1 µg/ml ionomycin for 10 min. Colocalization of NFAT and DAPI fluorescence assessed by similarity score analysis from *n*=5 independent experiments is shown.

(**E**) Expression of CD44 and CD25 in naïve CD4+ T cells from XPR1 cKO (red) and CTL (blue) mice after anti-CD3/anti-CD28 stimulation for three days; representative flow cytometry histograms with unstained control in gray is shown; *n*=5.

(**F**) IL-2 concentration of supernatants from XPR1 cKO and CTL CD4+ T cells stimulated as in (e); *n*=3.

Values are expressed as mean ± SEM; statistical significance is indicated as *$p < 0.05$, **$p < 0.01$, ***$p < 0.001$. Unpaired Student *t* test (B-F) was performed for statistical analysis.

Figure 3

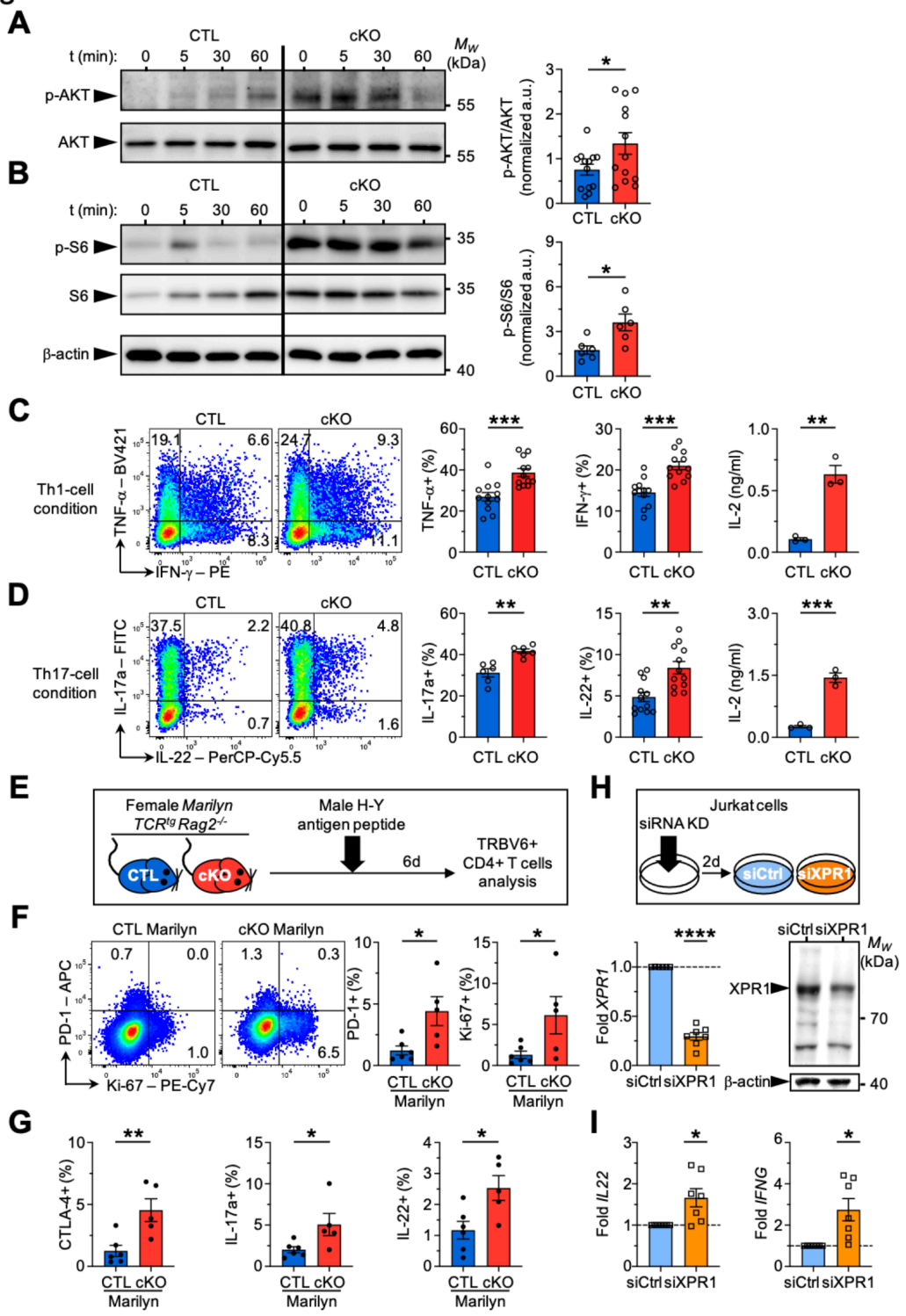


Figure 3

Xpr1 deficiency promotes AKT/mTOR signaling and cytokine production.

(**A** and **B**) Phosphorylation of AKT (p-AKT) and S6 (p-S6) in naïve CD4+ T cells from XPR1 cKO and CTL mice after stimulation with 5 μg/ml anti-CD3 for indicated time; quantification after 5 min stimulation of

normalized p-AKT/AKT ratio from *n*=13 and normalized p-S6/S6 ratio from *n*=6 independent experiments are shown.

(**C** and **D**) Representative flow cytometry plots, quantification of cytokine expression and corresponding IL-2 levels of *in vitro* differentiated CD4+ T cells from XPR1 cKO and CTL mice under (c) Th1-skewing and (d) Th17-skewing conditions; FACS analysis *n*=12 (TNF-a, IFN-g, IL-22), *n*=6 (IL-17a) and ELISA *n*=3.

(**E**) Experimental overview to assess XPR1-dependent antigen-specific T-cell responses *in vivo* by injection of male H-Y antigen peptide into female XPR1 cKO and CTL *Marilyn*mice.

(**F** and **G**) Representative flow cytometry plots and quantification of (f) PD-1 and Ki-67 expression and (g) CTLA-4, IL-17a and IL-22 expression of TRBV6+CD4+ T cells from antigen-injected XPR1 cKO and CTL *Marilyn* mice in *n*=5 independent experiments.

(**H** and **I**) Experimental overview to assess altered expression in Jurkat cells with siRNA-mediated knockdown (KD) of *XPR1* (upper panel). Transcript inhibition of *XPR1* and reduced XPR1 expression levels (lower panel) and (i) elevated cytokine transcription in siXPR1-treated Jurkat cells normalized to siCtrl-treated samples; *n*=7.

Values are expressed as mean ± SEM; statistical significance is indicated as *$p < 0.05$, **$p < 0.01$, ***$p < 0.001$, ****$p < 0.0001$. Unpaired Student *t*test (A-G) and One-sample *t* test (H,I) was performed for statistical analysis.

Figure 4

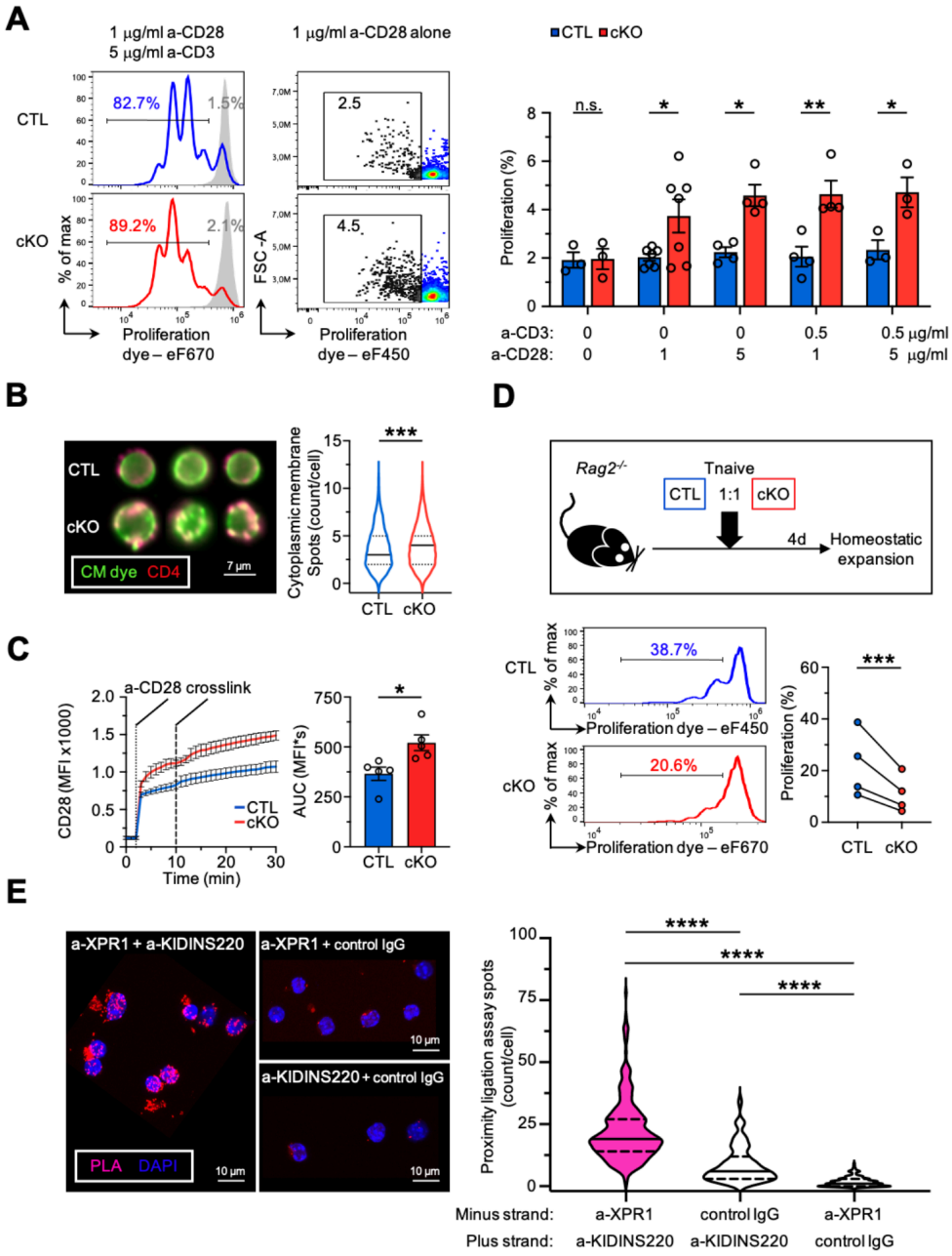


Figure 4

XPR1 restricts CD28 costimulation.

(**A**) Proliferation of CD4+ T cells from XPR1 cKO and CTL mice without (in gray) and with sufficient anti-CD3/anti-CD28 stimulation (color lines) depicted in histograms or in response to anti-CD28 stimulation

alone (dot plots). Quantification of proliferative responses towards anti-CD28 stimulation without or with suboptimal anti-CD3 stimulation as indicated; *n*=3, 7, 4, 4 and 3, respectively.

(**B**) Representative images of membrane rearrangement of naïve CD4+ T cells from XPR1 cKO and CTL mice TCR-stimulated for 90 min and stained with Cellbrite cytoplasmatic membrane dye. Population analysis from one out of two experiments performed with built-in spot count feature of IDEAS is shown with *n*=1602 (CTL) and *n*=1712 (cKO) T cells.

(**C**) Kinetic of CD28 surface clustering and AUC for CD28-stimulated CD4+ T cells from XPR1 cKO and CTL mice from *n*=5 independent experiments.

(**D**) Equal numbers of naïve CD4+ T cells from XPR1 cKO and CTL mice labelled with distinct proliferation dyes were adoptively transferred into *Rag2*$^{-/-}$ mice. Representative histograms and quantification of homeostatic expansion after four days is shown for *n*=4 recipients.

(**E)** Representative confocal microscopy images and spot quantification in CD4+ T cells stained for XPR1-KIDINS220 association by proximity ligation assay (PLA) and DAPI. Analysis of CD4+ T cells stained with both specific IgGs (a-XPR1 with a-KIDINS220, *n*=281) and each specific IgG in combination with respective control IgGs (a-XPR1 with control IgG, *n*=153; a-KIDINS220 with control IgG, *n*=107) from three independent experiments are shown.

Values are expressed as mean ± SEM; statistical significance is indicated as *p< 0.05, **p < 0.01, ***p < 0.001, ****p< 0.0001; not significant (n.s.). 2-way ANOVA followed by Sidak multiple comparisons test (A), Mann-Whitney test (B), unpaired Student *t* test (C), paired Student *t* test (D) and Kruskal-Wallis ANOVA followed by Dunn multiple comparisons test (E) was performed for statistical analysis.

Figure 5

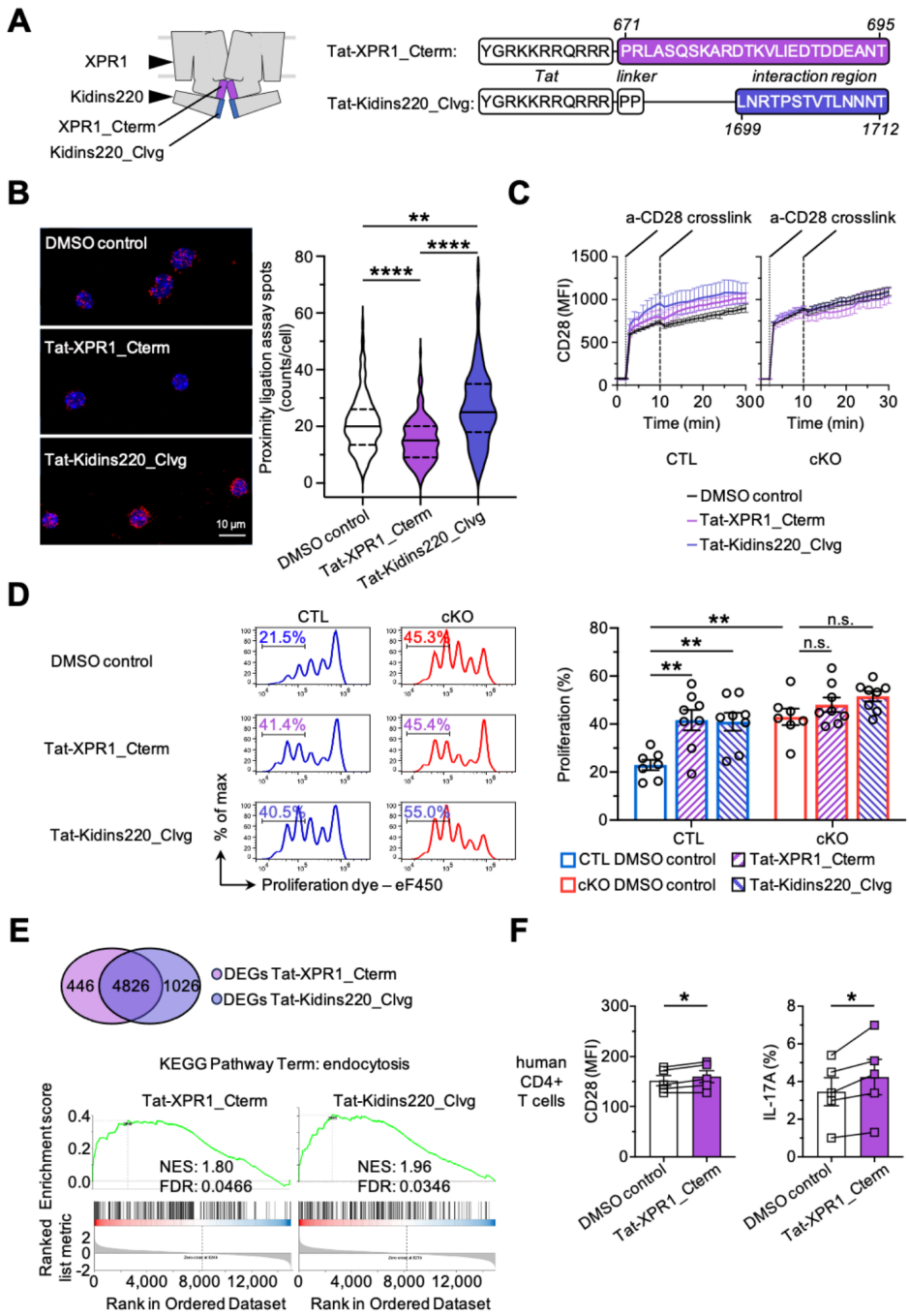


Figure 5

XPR1-KIDINS220 interaction regulates CD28 costimulation through endocytosis.

(**A**) Schematic complex organization of XPR1 and KIDINS220 with C-terminal binding region and cleavage site, respectively. Membrane-permeable peptide constructs of Tat-XPR1-Cterm for XPR1

binding competition and Tat-KIDINS220-Clvg for KIDINS220 degradation protection, derived from NP_035403.1 and NP_001074847.1 protein sequences, respectively, are shown.

(**B**) Representative confocal microscopy images and spot quantification in CD4+ T cells treated with DMSO vehicle control (*n*=281), Tat-XPR1-Cterm (*n*=220) or Tat-KIDINS220-Clvg (*n*=130) prior to staining of XPR1-KIDINS220 association by proximity ligation assay (PLA) and DAPI from three independent experiments.

(**C**) Kinetic of CD28 surface clustering on CD4+ T cells from XPR1 cKO and CTL mice treated with DMSO vehicle control, Tat-XPR1-Cterm or Tat-KIDINS220-Clvg before stimulation with anti-CD28 (a-CD28) and crosslinking antibodies; *n*=4 (CTL) and *n*=3 (cKO).

(**D**) Representative histograms and proliferation quantification in bar graphs of stimulated CD4+ T cells from XPR1 cKO and CTL mice after treatment with DMSO vehicle control (*n*=7), Tat-XPR1-Cterm (*n*=8) or Tat-KIDINS220-Clvg (*n*=8).

(**E**) Venn diagram of DEGs overlap for Tat-XPR1-Cterm and Tat-KIDINS220-Clvg in comparison to DMSO vehicle control treatment from CD4+ T cells stimulated for three days; *n*=3. Gene set enrichment analysis of shared targets for both protein transductions demonstrating contribution to endocytosis pathway regulation; normalized enrichment score (NES) and false discovery rate (FDR) are shown.

(**F**) Surface expression of CD28 and IL-17A production of human naïve CD4+ T cells treated with Tat-XPR1-Cterm in comparison to DMSO control treatment before anti-CD3/anti-CD28 stimulation for four days.

Values are expressed as mean ± SEM; statistical significance is indicated as *$p < 0.05$, **$p < 0.01$, ****$p < 0.0001$; not significant (n.s.). Kruskal-Wallis ANOVA followed by Dunn multiple comparisons test (B), One-way ANOVA followed by Tukey multiple comparisons test (D) and paired Student *t* test (F) was performed for statistical analysis.

Supplementary Files

This is a list of supplementary files associated with this preprint. Click to download.

- SupplementaldataMengel.pdf
- MengelSupplementaryuncropped.pdf